The Astrophysical Journal, 837:19 (8pp), 2017 March 1 https://doi.org/10.3847/1538-4357/aa5ea4

The *Chandra* COSMOS Legacy Survey: Energy Spectrum of the Cosmic X-Ray Background and Constraints on Undetected Populations

Nico Cappelluti[1,2,3], Yanxia Li[1,2,3,4], Angelo Ricarte[3], Bhaskar Agarwal[1,2,3], Viola Allevato[5], Tonima Tasnim Ananna[1,2,3], Marco Ajello[6], Francesca Civano[7], Andrea Comastri[8], Martin Elvis[7], Alexis Finoguenov[5,9], Roberto Gilli[8], Günther Hasinger[4], Stefano Marchesi[6], Priyamvada Natarajan[1,2,3], Fabio Pacucci[2], E. Treister[10], and C. Megan Urry[1,2,3]
[1] Yale Center for Astronomy and Astrophysics, P.O. Box 208121, New Haven, CT 06520, USA
[2] Department of Physics, Yale University, P.O. Box 208121, New Haven, CT 06520, USA
[3] Department of Astronomy, Yale University, P.O. Box 208101, New Haven, CT 06520, USA
[4] Institute for Astronomy, 2680 Woodlawn Drive, University of Hawaii, Honolulu, HI 96822, USA
[5] Department of Physics, University of Helsinki, Gustaf Hällströmin katu 2a, FI-00014 Helsinki, Finland
[6] Department of Physics and Astronomy, Clemson University, Kinard Lab of Physics, Clemson, SC 29634-0978, USA
[7] Harvard-Smithsonian Center for Astrophysics, 60 Garden Street, Cambridge, MA 02138, USA
[8] INAF-Osservatorio Astronomico di Bologna, via Ranzani 1, I-40127 Bologna, Italy
[9] Max-Planck-Institut für extraterrestrische Physik, Postfach 1312, D-85741, Garching bei München, Germany
[10] Instituto de Astrofisica, Facultad de Fisica, Pontificia Universidad Catolica de Chile, Casilla 306, Santiago 22, Chile
Received 2016 June 13; revised 2017 January 26; accepted 2017 February 3; published 2017 February 28

Abstract

Using *Chandra* observations in the 2.15 deg^2 COSMOS-legacy field, we present one of the most accurate measurements of the Cosmic X-ray Background (CXB) spectrum to date in the [0.3–7] keV energy band. The CXB has three distinct components: contributions from two Galactic collisional thermal plasmas at $kT \sim 0.27$ and 0.07 keV and an extragalactic power law with a photon spectral index $\Gamma = 1.45 \pm 0.02$. The 1 keV normalization of the extragalactic component is 10.91 ± 0.16 keV cm^{-2} s^{-1} sr^{-1} keV^{-1}. Removing all X-ray-detected sources, the remaining unresolved CXB is best fit by a power law with normalization 4.18 ± 0.26 keV cm^{-2} s^{-1} sr^{-1} keV^{-1} and photon spectral index $\Gamma = 1.57 \pm 0.10$. Removing faint galaxies down to $i_{\rm AB} \sim 27$–28 leaves a hard spectrum with $\Gamma \sim 1.25$ and a 1 keV normalization of $\sim$1.37 keV cm^{-2} s^{-1} sr^{-1} keV^{-1}. This means that $\sim$91% of the observed CXB is resolved into detected X-ray sources and undetected galaxies. Unresolved sources that contribute $\sim$8%–9% of the total CXB show marginal evidence of being harder and possibly more obscured than resolved sources. Another $\sim$1% of the CXB can be attributed to still undetected star-forming galaxies and absorbed active galactic nuclei. According to these limits, we investigate a scenario where early black holes totally account for non-source CXB fraction and constrain some of their properties. In order to not exceed the remaining CXB and the $z \sim 6$ accreted mass density, such a population of black holes must grow in Compton-thick envelopes with $N_H > 1.6 \times 10^{25}$ cm^{-2} and form in extremely low-metallicity environments $(Z_\odot) \sim 10^{-3}$.

Key words: catalogs – infrared: diffuse background – quasars: supermassive black holes – surveys – X-rays: diffuse background

1. Introduction

Focusing X-ray telescopes like *ROSAT*, *Chandra*, *XMM-Newton*, and *Swift* have shown that the main contributors to the extragalactic Cosmic X-ray Background (CXB) are Active Galactic Nuclei (AGNs). Although the spectrum of the CXB has been measured by almost every X-ray telescope, measurements vary significantly in the [0.3–10] keV energy band. The actual normalization of the CXB spectrum is therefore still a matter of debate, and this uncertainty leaves systematic uncertainties in AGN population synthesis models (Gilli et al. 2001; Treister & Urry 2005; Gilli et al. 2007; Treister et al. 2009). An important tool to fully understand the nature of the CXB is the unresolved CXB spectrum, once faint X-ray and optical/NIR sources have been removed. Thanks to its excellent angular resolution, *Chandra* can resolve faint sources in deep exposures, which can then be excised. This allows us to study both the X-ray stacked spectrum and the remaining CXB flux.

Previous mission measurements agree that the CXB spectral index is $\Gamma \sim 1.4$ but the normalization is uncertain by $\sim$20%–30%. These discrepancies are likely due to inaccurate spectral cross-calibrations, poorly understood instrumental backgrounds, and cosmic variance (Moretti et al. 2009). Another significant limitation in determining the amplitude of the soft extragalactic CXB is the ability to remove contamination from galactic components that peak below 2 keV where the effective area of focusing X-ray telescopes peaks. This poses a serious challenge to the understanding of the true fraction of unresolved soft CXB.

Recent papers suggest that the unresolved CXB may contain important information on the first generation of massive black holes in the universe (Cappelluti et al. 2012, 2013; Salvaterra et al. 2012; Kashlinsky 2016). Although deep surveys provide an estimate of the fraction of unresolved CXB via the integration of number counts (Moretti et al. 2003; Worsley et al. 2004; Hickox & Markevitch 2007; Moretti et al. 2012), the spectrum of the unresolved background has never been measured with sufficiently deep and wide surveys. Hickox & Markevitch (2006, 2007) successfully removed local foregrounds to make this measurement in the *Chandra* deep fields, but the limited size of the fields meant it was cosmic variance limited at the 20%–30% level. This impels us to carefully study the unresolved CXB with the highest degree of accuracy currently permitted by data.

In this paper, we make use of the best available data set, which is the largest deep survey ever performed by *Chandra*: the COSMOS-Legacy survey (Elvis et al. 2009; Civano et al.

2016; Marchesi et al. 2016). Here, we present a novel precise measurement of the CXB, its unresolved fraction, and new constraints on the properties of $z > 6$ black holes by using the Soltan argument.

2. Data set and Analysis

The *Chandra* COSMOS-Legacy survey (CCLS; Elvis et al. 2009; Civano et al. 2016) is an X-ray Visionary Program that imaged the 2.2 deg^2 COSMOS field (Scoville et al. 2007b) for a total of 4.6 Ms. The survey has an effective exposure of 160 ks over the central 1.5 deg^2 and ∼80 ks elsewhere. A total of 4016 X-ray sources are detected down to flux limits of 2.2×10^{-16}, 1.5×10^{-15}, and 8.9×10^{-16} erg cm^{-2} s^{-1} in the [0.5–2], [2–10], and [0.5–10] keV energy bands, respectively.

All the observations were performed in the VFAINT telemetry mode since it allows a lower instrumental background value. Here we briefly summarize our analysis, the details of which were mostly reported by Civano et al. (2016) and Puccetti et al. (2009). Level 1 data products were processed with the CIAO tool *chandra_repro*, retaining only valid event grades. Astrometry in each pointing was matched with the optical catalogs of Capak et al. (2007) and Ilbert et al. (2009). Particle background flares were removed using the *deflare* tool in compliance with the ACIS background analysis requirement after excising from the data set. In order to minimize uncertainties in modeling the quiescent particle background, we took special precautions to ensure that background flares were removed in a such a way that residuals from undetected faint flares were reduced. As shown in Hickox & Markevitch (2006), the [2.3–7] keV energy range is the most sensitive to particle background flares, and stowed-mode observations demonstrate that the [2.3–7] keV to [9.5–12] keV Hardness Ratio (HR) is constant. They also show that filtering the data for flares only in the [2.3–7] keV energy band results in missed periods of time during which the background has an anomalous HR. To account for this effect, we searched for flares not only in the [2.3–7] keV energy band, but also in the [9.5–12] and [0.3–3] keV bands. These "flared" time intervals were removed from the data (Cappelluti et al. 2009). With this procedure, we are confident that the remaining level of flaring is below 1%–2% (Hickox & Markevitch 2006), and therefore the amplitude of the quiescent particle background is subject to this level of systematic uncertainty. The *Chandra* X-ray Center (CXC) ACIS calibration team verified the validity of these assumptions, and no background anomalies have been reported as of 2016 May.

X-ray source masking and/or stacking was performed to match the Civano et al. (2016) X-ray source catalog. For X-ray undetected galaxies, we used the Scoville et al. (2007a) catalog of ∼1 million detections by the *Hubble Space Telescope* down to $m_{AB} \sim 27$–28 in the *i*-band. This enables a robust removal of faint X-ray undetected galaxies. Although Ilbert et al. (2009) and Laigle et al. (2016) assembled a catalog of ∼2 million galaxies, using these catalogs would have vastly reduced the area of our spectral extraction (see below) and made comparison with previous works more difficult. Moreover, for these last two catalogs, the coverage and sensitivities are uneven on the whole survey area.

2.1. Spectral Extraction

To obtain the spectrum of the full CXB, we use the entire ACIS-I area to maximize the collecting and survey area. This allows us to obtain a measurement that is minimally affected by poor statistics or cosmic variance. We call the spectrum of all photons detected in the field of view (FOV) the CXB spectrum.

However, to extract the *unresolved* CXB spectrum, we more carefully select the area used. Both *Chandra*'s point-spread function (PSF) and effective area rapidly degrade with the off-axis angle. Consequently, at large off-axis angles, little to no usable area is left after excising detected sources. The *Chandra* PSF radius can be approximated with: $r_{90} \sim 1'' + 10''(\theta/10')^2$, where r_{90} is 90% Encircled Energy Radius and θ is the off-axis angle. Compromising the need to maximize photon count with the degradation of our observations with the off-axis angle, we found that the highest quality data can be obtained using the inner 5′ ($\theta = 5' \Rightarrow r_{90} < 3\farcs5$).

To estimate the spectrum of the CXB after removing X-ray sources, we extracted the spectrum of the area remaining in the inner 5′ after removing the sources detected by Civano et al. (2016) using a 7″ radius region around each X-ray centroid. This radius corresponds to twice r_{90}, which we consider large enough to neglect the flux of the PSF tails. Because of the mosaicking, with these choices we still cover most of the CCLS area and mask 3% of the pixels because of sources. This spectrum will be called uCXB (unresolved CXB). According to Figure 2 of Civano et al. (2016), and thanks to the tiling of the pointings, this radius safely includes almost the totality of the source fluxes even without limiting the investigation to the inner FOV. Note that the *Chandra* PSF is not circular but is elongated as a function of the azimuthal angle. Nevertheless, we were able to use circular apertures because the asymmetry of the PSF is washed out by the tiling of the survey, which averages over azimuthal angles. See, e.g., the treatment of PSF fitting in Cappelluti et al. (2016).

To further probe the unknown discrete source CXB (hereafter nsCXB, non-source CXB), we extracted the spectrum of the area left after removing X-ray sources and *HST*-ACS-detected sources. These sources are so plentiful that using a 3.″5 masking radius leaves little sky area to perform our measurement. For this reason, we used the approach of Hickox & Markevitch (2007) and limited the search to the inner 3.′2 of axis of every pointing. We estimated that $r_{90} < 2\farcs2$, and masked areas around each galaxy of the Scoville et al. (2007b) catalog. The choice of this radius is a trade-off, ensuring that a large fraction of the X-ray flux of the optical-/NIR-selected galaxies is removed and keeping the contamination from PSF tails under control (see below for the treatment of PSF tails).

For each subsample, the net extracted counts are reported in Table 1. Remarkably, the CXB spectrum we derive contains ∼123,000 net counts. For each spectrum, we also computed the field-averaged Redistribution Matrix Functions (RMFs) and Ancillary Response Functions (ARF) using the CIAO tool *specextract*. Spectra were then co-added and response matrices averaged after weighting by the exposure time.

2.2. Background Treatment and Systematics

In this analysis, we assumed that the only background components were the particle background and detector noise. ACIS-stowed observations were taken for about 1 Ms. In this mode, the detector records the particle background and detector noise. We searched the Calibration Data Base (CALDB) for observations taken during the period proximate to our observations, with the same chips and tailored ACIS background event files to each of our observations. For each pointing, we

Table 1
Spectral Analysis Results

Sample	Net Counts cts	K_{PL} ph cm^{-2} s^{-1} sr^{-1}	Γ keV	kT_1 keV	kT_2	χ^2/dof
CXB	123948	10.91 ± 0.16 (±0.26)	1.45 ± 0.02 (±0.03)	$0.27^{+0.02}_{-0.02}$ ($^{+0.03}_{-0.04}$)	0.07 ± 0.01(±0.02)	191.71/208
uCXB	44642	4.18 ± 0.26 (±0.41)	1.57 ± 0.10 (±0.16)	0.22 ± 0.03 (±0.06)	$0.08^{+0.03}_{-0.01}$ ($^{+0.04}_{-0.03}$)	272.3/208
nsCXB	11034	1.37 ± 0.30 (±0.45)	1.25 ± 0.35 (±0.62)	0.22 ± 0.04 (±0.05)	…[a]	162/105

Note.
In parentheses are the 90% confidence limits.
[a] not required.

re-projected the stowed observation to the same observed *wcs* frame using the CIAO tool *reproject_events*; we verified that the stowed background events were calibrated with the same GAINFILE of our observations, and we ensured that the proper gain was used for all the "stowed" pointings. After these procedures we extracted the particle background spectra in the same areas described above (corresponding to the CXB, uCXB, and nsCXB regions).

Hickox & Markevitch (2006, 2007) found that the spectral shape of the *Chandra* background is extremely stable in time and can be easily modeled for extended and diffuse emission like the CXB, by using ACIS observations taken in stowed mode. As mentioned above, the shape of the particle background spectrum is constant in time but its amplitude is not. We scale it by the ratio of the count rate in the [9.5–12] keV data (where no astrophysical events are recorded) to that in the stowed data. These ratios vary from 0.79–1.15. With this procedure, the systematic uncertainty on the background estimation is ∼2% (Hickox & Markevitch 2006). We averaged the background spectra of each pointing to take into account the different locations of the masked sources. We also subtracted out of time events (counts accumulated during readouts) that account for <1% of the total events. When using χ^2 statistics, XSPEC is capable of handling systematic errors while fitting the data and adding them to the error budget. Therefore, by using the tool *grppha*, we included a 2% systematic in the stowed-background spectrum. Moreover, Leccardi & Molendi (2007) and Humphrey et al. (2009) report that the use of χ^2 or CSTAT could produce biased results in the high-counts regime. According to Table 1 we expect a <2% bias in the fit results. We have factored an additional 2% systematic into our fits, for a total of ∼4% of systematics.

Although an actual risk of underestimating the background does exist, at the 1%–2% level, this risk has been mitigated by treating the flares according to their hardness ratios. Without considering the 2% systematics, the fit does not change significantly. This is because the error budget is dominated by the intrinsic Poissonian error, associated with the stowed background, which has been estimated by accumulating one-third fewer photons than the real observation. This is clearly visible in Figure 1 where we compare the nsCXB spectrum and the PIB spectrum. There one can clearly note how the uncertainties are dominated by the statistical error on the PIB spectrum.

Due to the uncertain background subtraction near instrumental emission lines, which may suffer from uncertainties of the order 5%–10% (Bartalucci et al. 2014), we limit our analysis to the [0.3–7] keV band and exclude the 2.0–2.4 keV energy range (which contains instrumental Au $M_{\alpha\beta}$ lines).

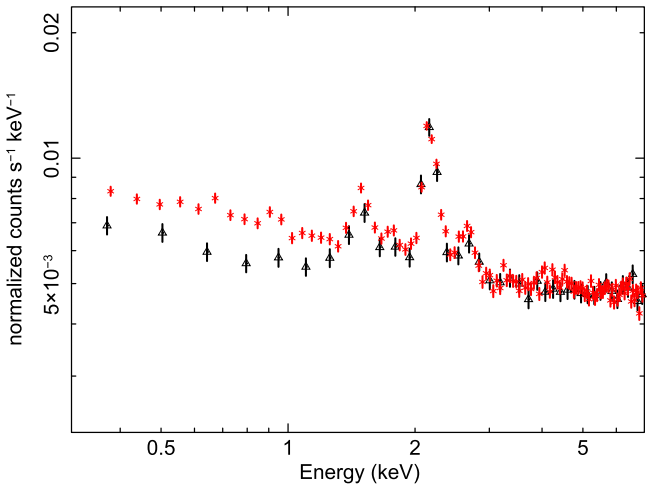

Figure 1. Comparison of the nsCXB (red stars) before background subtraction and the PIB (black triangles). It is worth noting that the error bars of the PIB spectrum are much larger that those of the raw nsCXB spectrum.

2.3. Spectral Fitting

The observed spectra are shown in Figure 2. We fitted the observed X-ray spectra, grouped in bins of two channels, using XSPEC v12.9 (Arnaud 1996). In total the CXB and uCXB spectra have 213 spectral bins while the nsCXB has 98. The full [0.3–7] keV CXB consists of three principal components (Miyaji et al. 1998): (a) an extragalactic component produced by the integrated emission of resolved and unresolved discrete sources (AGNs, galaxies, and clusters), which we model as a power law (hereafter PL) times Galactic absorption with $N_H = 2.0 \times 10^{20}$ cm^{-2} (Dickey & Lockman 1990); for the absorption we used the *tbabs* model in XSPEC with cross-sections form Verner et al. (1996) and abundances from Wilms et al. (2000). (b) A Galactic hot gas component with a temperature of the order $kT \sim 0.15$–0.25 keV, which we model using moderately absorbed (i.e., $N_H = N_{H,\mathrm{Gal}}$) emission from collisionally ionized diffuse gas (APEC, hereafter A1), known as the hard thermal component of the of the IGM whose temperature and intensity is a strong function of the galactic coordinates (see, e.g., Markevitch et al. 2003). (c) A lower temperature local bubble and/or geocorona, previously known as soft thermal CXB, modeled with an unabsorbed APEC hereafter A2). For these CXB components, we varied the following parameters: spectral Index Γ, PL normalization K_{PL}, A1 and A2 normalizations, and temperature kT. N_H was fixed for both PL and A1. Abundances were set to solar for both A1 and A2.

However, we note that the temperatures and amplitudes of the soft components are slightly degenerate with the power-law

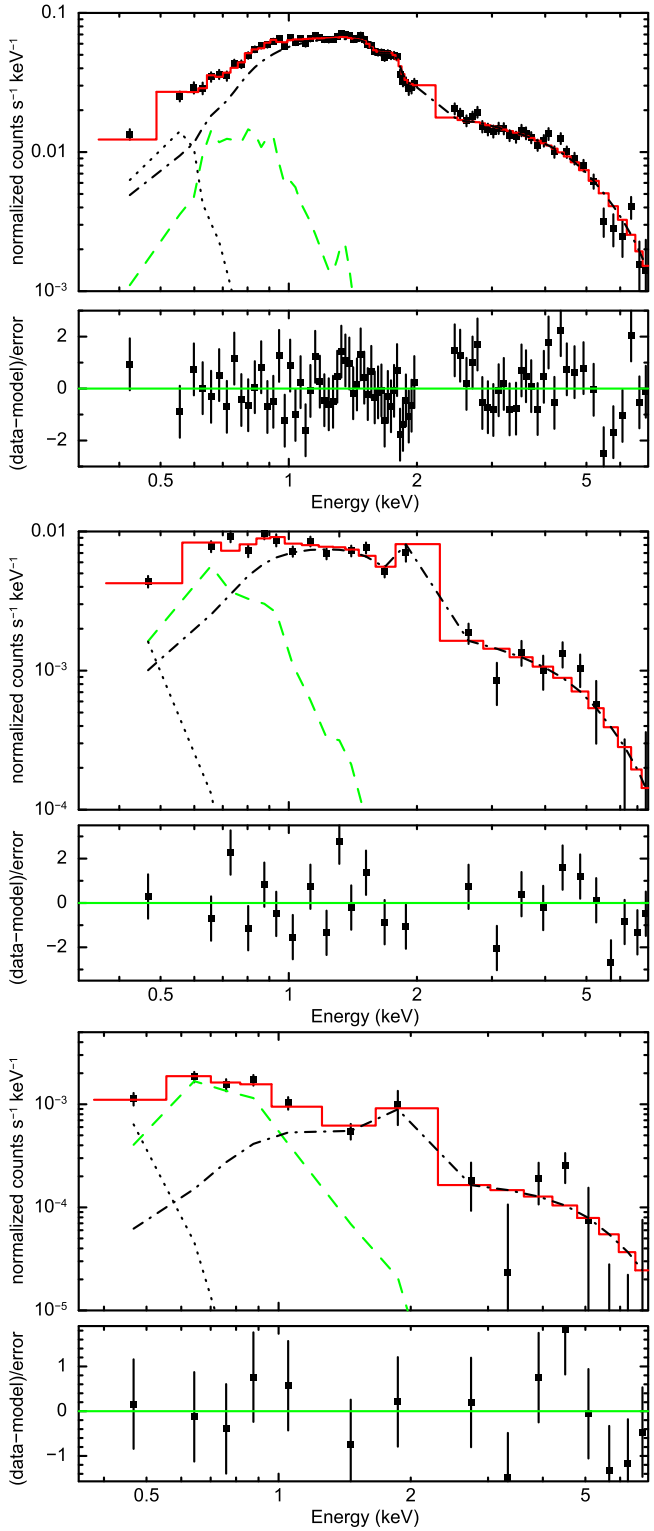

Figure 2. From top to bottom, the binned CXB, uCXB, and nsCXB folded spectra, respectively. Black squares are the data points. The red continuous line is the best-fit model, the dotted–dashed line is the extragalactic components, the green dashed line is the hard thermal component, and the dotted line is the local bubble components. In the bottom panels we show the fit residuals. Data have been re-binned in order to have at least 10σ significance per bin and no more than 20 bins have been combined.

slope. To be conservative, we kept them free to vary in the fit. Moreover, on scales of several arcmin, there might be fluctuations in temperature and amplitude that we want to take into account because of the different sizes of the field of view employed for analyzing every subcomponent of the CXB.

3. Results

3.1. Overall CXB Spectrum

The CXB spectrum, the best-fit model, and its components are shown in Figure 2. The best-fit parameters are summarized in Table 1. The foreground local components have measured temperatures $kT \sim 0.27$ keV and $kT \sim 0.07$ keV, respectively. Both components are required at high significance level. Indeed, for our fit $\chi^2/\mathrm{dof} = 191.71/208$ but if we remove the local bubble (soft thermal) component we obtain $\chi^2/\mathrm{dof} = 231.62/208$. We performed an *f*-test and, as a result, we found that the soft component is required at a 4.7σ level. If we remove the hard thermal component, the fit converges on a single power-law model but with $\chi^2/\mathrm{dof} \gg 2$. Above 2 keV, the emission can be totally ascribed to the extragalactic power-law component. The latter has a photon spectral index $\Gamma = 1.45 \pm 0.02$, as in previous investigations (see, e.g., Gruber et al. 1999; Ajello et al. 2008) and a normalization $K_{\mathrm{PL}} = 10.91 \pm 0.16$, consistent with previous *Chandra* (Hickox & Markevitch 2006), *Swift* (Ajello et al. 2008; Moretti et al. 2009), and *ROSAT*-ASCA results (Miyaji et al. 1998), yet lower than the early *XMM-Newton* (De Luca & Molendi 2004) and higher than the ASCA and *HEAO* results (Gendreau et al. 1995; Gruber et al. 1999). This CXB unfolded spectrum is compared with these previous measurements in Figure 3. Due to the pencil beam nature of the survey, rare bright sources are not accounted for in our measurement. A precise estimate of their contribution is not possible with the data in hand, but using AGN population synthesis models (Gilli et al. 2007; Treister et al. 2009) we estimate that our measurement of the full CXB is underestimated by 3%. We rather not consider this to be a systematic error, but a limitation of our total CXB measurement. We have also measured the overall flux of the CXB in several energy bands and reported it in Table 2. The thermal contributions are dominant below 1 keV and account for about 23% of the overall [0.5–2] keV flux. The remainder of the flux can be ascribed to extragalactic emission, while above 2 keV most of the signal is extragalactic. The intensity of the Galactic components is in remarkable agreement with the micro-calorimeter measures of McCammon et al. (2002).

3.2. X-Ray Source Masked CXB Spectrum and Flux

The uCXB, which is shown in Figure 2, has a slightly softer spectrum ($\Gamma \sim 1.57$) than the overall component (CXB), but still consistent with it. The Galactic foregrounds have, within the uncertainties, the same intensity and shape as the CXB. The uCXB spectrum is shown in Figure 5. Even in this case we obtain an excellent fit with three components with $\chi^2/\mathrm{dof} = 272.3/208$. The slightly softer spectral slope is consistent with the observed higher fraction of Type I AGNs among the brightest sources. In Table 3 we show the fraction of resolved CXB as a function of energy. The removal of X-ray sources produces a drop on the remaining surface brightness of the CXB of about 70%–80% regardless of the energy. This is not an impressive fraction because of the CCLS flux limit, but we can compensate for the shallow depth of the survey by searching through what is left after masking faint *HST* sources.

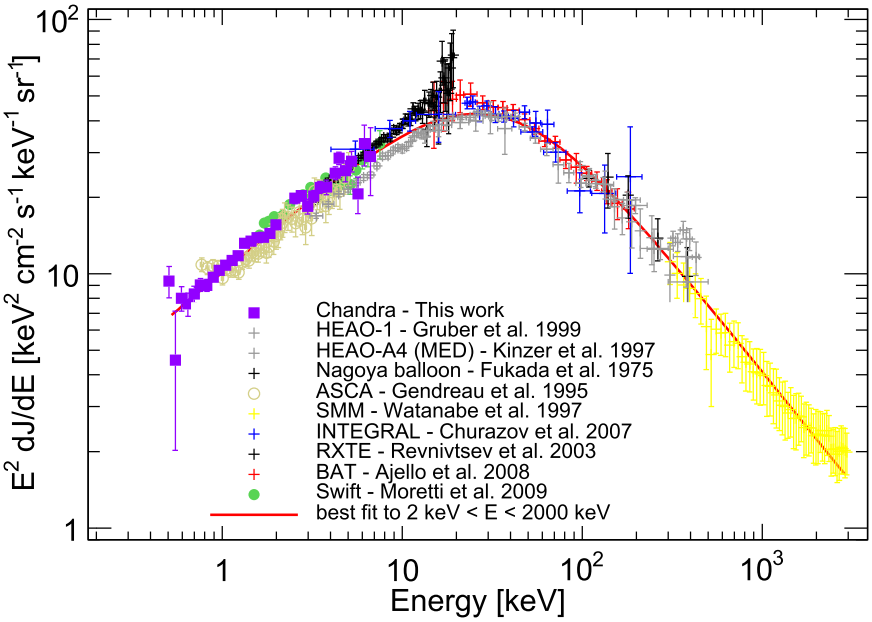

Figure 3. Magenta squares are the full CXB measured in this work using *Chandra* data from the COSMOS field (with local soft components subtracted), compared with previous results over the 0.3–1000 keV energy range and the best fit of Ajello et al. (2008). Green circles are from Moretti et al. (2009), gray crosses are the HEAO–1 measurements of Gruber et al. (1999) and Kinzer et al. (1997), red crosses are the *Swift–BAT* measurements from Ajello et al. (2008), black crosses are *RXTE* measurements from Revnivtsev et al. (2003), blue crosses are *INTEGRAL* measurements from Churazov et al. (2007), yellow crosses are SMM measurements from Watanabe et al. (1998), pale green open circles are *ASCA* measurements from Gendreau et al. (1995), and black crosses >100 keV are from the Nagoya balloon experiment of Fukada et al. (1975).

Table 2
CXB Fluxes

BAND keV	Total erg s^{-1} cm^{-2} deg^{-2}	Local erg s^{-1} cm^{-2} deg^{-2}	Extragal.
0.5–1.0	$5.38^{+0.16}_{-0.15}$	$2.56^{+0.18}_{-0.18}$	$3.13^{+0.07}_{-0.07}$
1.0–2.0	$4.55^{+0.03}_{-0.03}$	$0.05^{+0.01}_{-0.01}$	$4.52^{+0.05}_{-0.05}$
0.5–2.0	$9.95^{+0.16}_{-0.18}$	$2.29^{+0.23}_{-0.21}$	$7.62^{+0.11}_{-0.11}$
2.0–10.0	$20.34^{+0.05}_{-0.06}$	0	$20.34^{+0.05}_{-0.06}$

Note. In units of 10^{-12} erg s^{-1} cm^{-2} deg^{-2}.

Table 3
Unresolved Extragalactic CXB Fluxes

BAND keV	Extragal. erg s^{-1} cm^{-2} deg^{-2}	$\%_{CXB}$
uCXB		
0.5-1.0	1.24 ± 0.17	23.0 ± 3.2
1.0-2.0	1.66 ± 0.06	36.5 ± 0.1
0.5-2.0	2.90 ± 0.16	30.1 ± 1.7
2.0-10.0	6.47 ± 0.82	31.8 ± 4.0
nsCXB		
0.5-1.0	$0.36^{+0.13}_{-0.11}$	$6.7^{+3.0}_{-2.8}$
1.0-2.0	$0.61^{+0.07}_{-0.07}$	$13.4^{+1.6}_{-1.6}$
0.5-2.0	$0.97^{+0.18}_{-0.16}$	$9.7^{+1.6}_{-1.8}$
2.0-10.0	$3.45^{+1.42}_{-1.19}$	$17.0^{+5.9}_{-7.0}$

Note. In units of 10^{-12} erg s^{-1} cm^{-2} deg^{-2}.

3.3. Non-source CXB Spectrum

The extracted nsCXB cannot be directly used as is, since we know that up to 10% of the flux from galaxies is in the PSF tails and contaminates our results. We have therefore extracted the spectrum of all the galaxies inside the mask, fit it with a simple absorbed power-law model (properly taking into account the different thermal background components in the fit), and found a spectral slope $\Gamma \sim 1.3 \pm 0.06$ and normalization $K = 3.38 \pm 0.14$. We rescaled the normalization to take into account the fraction of flux falling out of the mask. Such a renormalization has been computed in the following way: we estimated, given a circular area of 3.′2, the area-weighted mean off-axis angle $\langle\theta\rangle = \frac{\int_0^{3.2'} \theta * \pi\theta^2 d\theta}{\int_0^{3.2'} \pi\theta^2 d\theta} = 2.'25$. At this off-axis angle, an average of 95% EEF is masked. Hence, we renormalized the galaxy spectrum by a factor of 0.95 and simulated a spectrum taken from the rescaled best fit, accounting for all the observational parameters. We subtracted the simulated spectrum from the nsCXB spectrum to remove the best possible estimate of PSF tails.

Due to lower statistics, to fit such a spectrum we doubled the binning with respect to the cases above. This is because we have chosen a binning that allowed having at least 30 counts/bin. In Figure 1 we show the spectrum of the nsCXB. The spectrum has high S/N up to an energy of 5–6 keV, above which the signal is very noisy. We allowed all parameters to vary freely, but because of the low statistics, the soft thermal component is detected but not significantly required. The resulting best-fit parameters are $\Gamma = 1.25 \pm 0.35$ and normalization $K_{\rm PL} = 1.37 \pm 0.30$. This corresponds to $9.7^{+1.6}_{-1.8}$% of the total CXB in the [0.5–2] keV band. This unresolved CXB fraction is about double above 2 keV. Our normalization of this unresolved component is in agreement with Hickox & Markevitch (2007) and Moretti et al. (2012), while our estimated slope is in agreement with Hickox & Markevitch (2007) but significantly softer than the Moretti et al. (2012) estimate. In Table 3 we show the extragalactic component flux of the nsCXB in several energy bands. With our masking, the

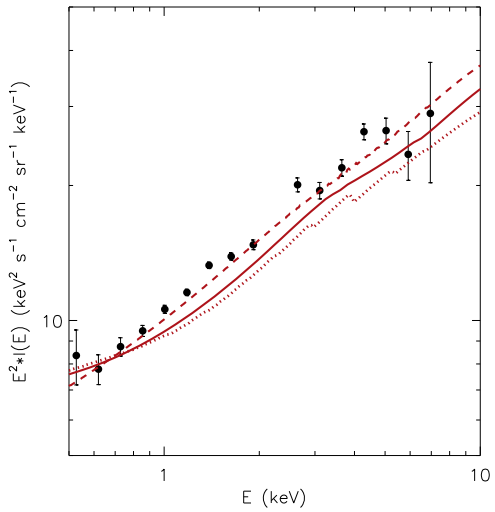

Figure 4. Unfolded CXB spectrum measured by *Chandra* with ACIS-I (*black*) in this work. Overplotted on the data we show AGN population synthesis models, after adding cluster emission (Gilli et al. 1999) and star-forming galaxy emission (Cappelluti et al. 2016) by Treister et al. (2009; red dotted line), Gilli et al. (2007; red continuous line), and Ballantyne et al. (2011; red dashed line). The extragalactic CXB spectrum is well fitted by a power-law model with photon index $\Gamma \sim 1.45$ and normalization $\sim$10.91 keV cm^2 s^{-1} sr^{-1}.

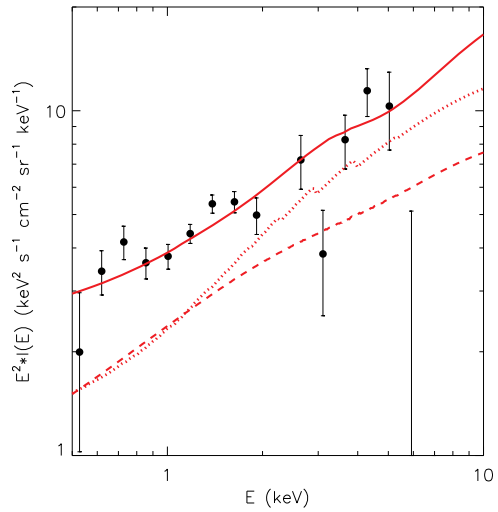

Figure 5. Spectrum of the uCXB (*circles*) as measured with *Chandra* ACIS-I in this work. The uCXB spectrum is compared with AGN synthesis models by Treister et al. (2009; red dotted line), Gilli et al. (2007; red continuous line) and Ballantyne et al. (2011; red dashed line) after the survey's X-ray-selection function is applied (galactic N_H correction is irrelevant).

fraction of CXB remaining varies between $\sim$6% at very soft energies to 17% at very high energies.

4. Discussion

Ordinary populations of Type I and Type II AGNs alone cannot explain the shape and amplitude of the extragalactic CXB spectrum, especially the peak at $\sim$30 keV (Comastri et al. 1995; Gilli et al. 2001; Treister & Urry 2005; Gilli et al. 2007; Treister et al. 2009; Ballantyne et al. 2011). Instead, this peak is attributed to a large population of mostly undetected Compton-thick sources that are naturally missed by $<$10 keV X-ray surveys.

In Figure 4 we compare our data with the predictions of the CXB AGN population synthesis models that have animated the scientific debate in the last 10 years (Treister & Urry 2005; Gilli et al. 2007; Treister et al. 2009; Ballantyne et al. 2011; Ueda et al. 2014). Star-forming galaxies were modeled by assuming a power law with photon index $\Gamma = 2$ and a normalization of 0.55 keV cm^2 s^{-1} sr^{-1} keV^{-1}, estimated using the prescription of Cappelluti et al. (2016, see below). In that figure, we present the extragalactic CXB unfolded spectrum; although such a plot is model dependent, this is still a good approximation for the purpose of comparing with the model. A cluster model component from Gilli et al. (1999) has been added to each of these spectra. The three models reproduce the shape of the extragalactic CXB spectrum above 0.5 keV but systematically underestimate the normalization by 10%–15%. This is likely due to the intrinsic normalization chosen as a reference for these models. Differences among the models are of the order of the precision of our measurement.

A valuable test of the goodness of the assumptions of population synthesis models derives from whether they are able to reproduce the uCXB at any given flux limit. In Figure 5 we compare the uCXB spectrum with the predictions of Treister et al. (2009), Gilli et al. (2007), and Ballantyne et al. (2011) at the flux limit of COSMOS (models assume an all-sky coverage, and we did not apply any correction for cosmic variance). Interestingly, the only model that reproduces the whole uCXB is the Gilli et al. (2007) one while that of Treister et al. (2009) is consistent with the hard X-rays. This consistency at high energy is not surprising since both models aimed to explain the peak of the CXB at high energy, and although they used different ingredients, they included a large number of hard, Compton-thick objects. The Ballantyne et al. (2011) model underpredicts the fraction of uCXB, implying that their model contains more bright sources than the other models. These discrepancies are likely due to the different assumptions for the N_H distribution and luminosity functions adopted. Given the quality of the CXB data we present here and the consistent CXB levels measured by *Chandra* and *XMM-Newton*, a new population synthesis model may be warranted.

According to our analysis, $\sim$8%–11% of the measured [0.5–2] keV CXB cannot be explained by either resolved X-ray sources or faint, unresolved sources originating in visible red galaxies that have escaped detection. Cappelluti et al. (2012, 2013) and Helgason et al. (2014) studied the fluctuations of the u/nsCXB in the deep CDFS and EGS, and concluded that these fluctuations arise from undetected groups and star-forming galaxies and a small fraction of AGNs. A detailed analysis of the fluctuations of the u/nsCXB will be presented in Li et al. (2017, in preparation). Here, we remove even fainter sources than Cappelluti et al. (2013) and Helgason et al. (2014), down to $i_{\rm AB} \sim$ 27–28. Assuming that all the diffuse emission from faint groups has been removed by our galaxy masking, what is left arises from very faint undetected/blurred point sources.

In order to evaluate the contribution of star-forming galaxies to the CXB and uCXB, we used simulations of the CANDELS GOODS-South area from Cappelluti et al. (2016), which reaches optical/NIR magnitudes as faint as 30. They predict for every galaxy a value of L_X concordant with the scaling relation with the SFR (approximated by the infrared luminosity) of Basu-Zych et al. (2013). Without going into details, they estimate $L_{8-1000\mu{\rm m}}$ using photo-z, star-formation rate, *UVJ* rest-frame colors, and (observed or extrapolated) UV luminosity (1500 Å). Using their mock catalog, we applied a selection as

similar as possible to that of Laigle et al. (2016) from which we derived our mask. As a result, we find that these galaxies produce a [0.5–2] keV CXB surface brightness of the order of 3.3×10^{-14} erg cm^2 s^{-1} deg^{-2}, which explains about 5% of the nsCXB. By assuming a typical X/O = 0 for AGNs as determined by Civano et al. (2012) and the *i*-limiting magnitudes in COSMOS (Scoville et al. 2007b), we estimate that the undetected AGN [0.5–2] flux is $<10^{-17}$ erg cm^2 s^{-1}. At these low fluxes, star-forming galaxies vastly outnumber AGNs, so we can assume that ordinary AGNs cannot contribute more than galaxies to the soft nsCXB (5%). Being so faint, the sources producing the remaining CXB can be local ($z \sim$ 1–3) and of low luminosity. Low-luminosity AGNs are preferentially highly absorbed (Barger et al. 2005; Hasinger 2008), and therefore we could argue that the hard portion of the nsCXB could be explained by these sources. However, at $z \sim 36$, the number density of absorbed sources is still unknown, and we cannot exclude an unpredicted large number of such sources at that redshift.

We propose that a large fraction of the remaining emission could arise from still undetected, rapidly accreting black holes at $z >$ 6–7. Assuming the Direct Collapse black hole (DCBH) scenario for the formation of early black hole seeds, Pacucci et al. (2015) showed that these sources are likely undetected in current deep X-ray/NIR surveys. They compared the emission of DCBHs for two accretion models: radiatively efficient (Standard) and radiatively inefficient (Slim Disk; super-Eddington), in which photon trapping is significant and the outgoing radiation is diminished. In the latter case, the luminosity emitted by these sources is low. These short-lived and fainter black holes are more difficult to detect compared to brighter objects accreting at the Eddington limit (two tentative detections were proposed by Pacucci et al. 2016). Indeed, Comastri et al. (2015) revised the estimate of the local accreted mass density by taking into account that a significant fraction of the local black holes may have grown by radiatively inefficient accretion. From our measurements, the maximum flux produced by accretion onto early black holes is ∼10% of the CXB (see Table 3).

To place limits on the amount of accretion occurring at $z \gtrsim 6$, we follow the formalism of Salvaterra et al. (2012), assuming that the comoving specific emissivity of AGNs can be factorized as

$$j(E, z) = j_\star f(z) g(E), \tag{1}$$

where $j_\star$ is the normalization, $f(z) = (1 + z)^{-\gamma}$, with $\gamma \approx 5$, is the redshift evolution, and $g(E)$ is a (normalized) template spectrum. For these templates, we use AGN spectra generated by realistic hydrodynamical simulations of accreting DCBHs (Pacucci et al. 2015). These templates allow us, essentially, to compute the bolometric correction needed for the Soltan argument as a function of redshift. For each value of the gas metallicity and accretion model (Standard or Slim Disk), we select the spectrum from the snapshot with the highest X-ray output. Combining Equation (1) with knowledge of the contribution to the background at energy E_0 by sources at redshifts $z \geqslant \bar{z}$, the normalization can be solved:

$$j_\star = \frac{4\pi J_{E_0} H_0 \Omega_m^{1/2}}{c} \left[\int_{\bar{z}}^{\infty} dz (1 + z)^{-5/2-\gamma} g(E_0(1 + z)) \right]^{-1}, \tag{2}$$

Table 4
Limits to the Density of Accretion at $z \gtrsim 6$ from the Unresolved Background

Accretion Disk	Metallicity ($Z_\odot$)	$\rho_\bullet$ ($M_\odot$ Mpc^{-3})
Standard	10^{-3}	6.1×10^3
Standard	10^{-2}	1.7×10^6
Slim Disk	10^{-3}	6.8×10^3
Slim Disk	10^{-2}	6.5×10^4

where J_{E_0} is the emissivity observed at energy E_0 today, and $j(E, z)$ on the other hand is the emissivity of all AGNs at redshift z. Note that E is in the rest frame, and E_0 is the energy observed at $z = 0$. Ω_m is the matter density parameter and H_0 is the Hubble constant.

The standard Soltan argument states that the mass density of accretion onto sources at redshifts $z \geqslant \bar{z}$ is given by

$$\rho_{\rm acc}(\bar{z}) = \frac{1 - \epsilon}{\epsilon c^2} \int_{\bar{z}}^{\infty} dz \frac{dt}{dz} \int_0^{\infty} dE j(E, z), \tag{3}$$

where ϵ is the radiative efficiency (0.1 and $\lesssim$0.04 for a standard and a slim disk, respectively. Finally, our limit on accretion at $z \geqslant \bar{z}$ is given by

$$\rho_{\rm acc}(\bar{z}) = \frac{4\pi J_{E_0}}{c^3} \frac{1 - \epsilon}{\epsilon} \left[\int_{\bar{z}}^{\infty} dz (1 + z)^{-5/2-\gamma} \right] \times \left[\int_{\bar{z}}^{\infty} dz (1 + z)^{-5/2-\gamma} g(E_0(1 + z)) \right]^{-1}. \tag{4}$$

Assuming that the unresolved 1.5 keV flux is entirely due to DCBHs at $z \gtrsim 6$, the inferred accretion density ($\rho_\bullet$) using these spectra is provided in Table 4. These limits are compared to those found in previous studies in Figure 6. Red, orange, green, and purple upper limits correspond to standard low-metallicity, slim disk low-metallicity, standard high-metallicity, and slim disk high-metallicity templates, respectively. In gray, we display limits from previous studies. The straight, dashed, dotted, and dotted–dashed error bars correspond to measurements from Hopkins et al. (2007), Salvaterra et al. (2012), Treister et al. (2009), and Treister et al. (2013), respectively. The gray square corresponds to local measurements by Shankar et al. (2009). Our results emphasize that limits to black hole accretion are dependent entirely on the bolometric correction assumed, and this can vary significantly from model to model. Again, while previous studies have assumed a constant fraction of total flux emitted in the observed window, we calculated this fraction directly from hydrodynamical simulations. These models imply that much less accretion is required to provide the observed flux if gas is accreted from a lower-metallicity reservoir $Z_\odot = 10^{-3}$, while larger metallicities $Z_\odot > 10^{-2}$ would exceed the $z \sim$ 5–6 accreted density of Hopkins et al. (2007). The limits in the lower-metallicity case are comparable to or more stringent than what is obtained with stacking analysis in Treister et al. (2013; $\rho_\bullet \lesssim 10^3 M_\odot$ Mpc^{-3}).

Cappelluti et al. (2013) determined that the unresolved nsCXB and unresolved cosmic infrared background fluctuations are highly correlated (see, e.g., Kashlinsky et al. 2012). Yue et al. (2013) interpreted this as a signature of emission from a population of DCBHs at $z >$ 12. In order to satisfy the observed cross-power and not to exceed the nsCXB measured

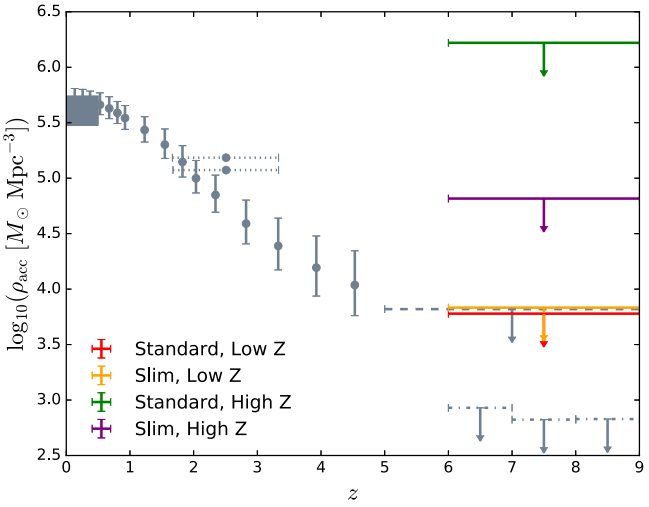

Figure 6. Comparison of our limits to previous studies. Red, orange, green, and purple bars represent our standard low-metallicity, slim disk low-metallicity, standard high-metallicity, and slim disk high-metallicity limits, respectively. In gray, the solid, dashed, dotted, and dotted–dashed error bars correspond to previous measurements by Hopkins et al. (2007), Salvaterra et al. (2012), Treister et al. (2009), and Treister et al. (2013). The gray square around redshift 0 corresponds to the local estimate by Shankar et al. (2009). Our study emphasizes that the assumed model dramatically changes the bolometric correction used, and therefore the limits on the accreted mass density.

here, their envelopes must be Compton-thick. With our new limits on the nsCXB, according to Yue et al. (2013) DCBHs must have $N_H > 1.6 \times 10^{25}\,\mathrm{cm}^{-2}$. To summarize, if this population of early massive black holes exists, the black holes had to grow in Compton-thick, low-metallicity environments.

N.C. acknowledges Yale University's YCAA Prize Postdoctoral fellowship. N.C., G.H., Y.L., and F.P. acknowledge the SAO *Chandra* grant AR6-17017B and NASA-ADAP grant MA160009. P.N. acknowledges support from a Theoretical and Computational Astrophysics Network grant with award number 1332858 from the National Science Foundation. B.A. and A.R. acknowledge support from the TCAN grant for a postdoctoral fellowship and a graduate fellowship, respectively. A.C. and R.G. acknowledge PRIN INAF 2014 Windy black holes combing galaxy evolution and ASI/INAF grant I/037/12/0 011/13. E.T. acknowledge support from FONDECYT regular grant 1160999 and Basal-CATA PFB-06. This work is part of the NASA Project "LIBRAE: Looking at Infrared Background Radiation Anisotropies with Euclid" (http://librae.ssaihq.com). We thank the anonymous referee for the useful insights and suggestions.

References

Ajello, M., Greiner, J., Sato, G., et al. 2008, ApJ, 689, 666
Arnaud, K. A. 1996, adass V, 101, 17
Ballantyne, D. R., Draper, A. R., Madsen, K. K., Rigby, J. R., & Treister, E. 2011, ApJ, 736, 56
Barger, A. J., Cowie, L. L., Mushotzky, R. F., et al. 2005, AJ, 129, 578
Bartalucci, I., Mazzotta, P., Bourdin, H., & Vikhlinin, A. 2014, A&A, 566, A25
Basu-Zych, A. R., Lehmer, B. D., Hornschemeier, A. E., et al. 2013, ApJ, 762, 45
Capak, P., Aussel, H., Ajiki, M., et al. 2007, ApJS, 172, 99
Cappelluti, N., Brusa, M., Hasinger, G., et al. 2009, A&A, 497, 635
Cappelluti, N., Comastri, A., Fontana, A., et al. 2016, ApJ, 823, 95
Cappelluti, N., Kashlinsky, A., Arendt, R. G., et al. 2013, ApJ, 769, 68
Cappelluti, N., Ranalli, P., Roncarelli, M., et al. 2012, MNRAS, 427, 651
Churazov, E., Sunyaev, R., Revnivtsev, M., et al. 2007, A&A, 467, 529
Civano, F., Elvis, M., Brusa, M., et al. 2012, ApJS, 201, 30
Civano, F., Marchesi, S., Comastri, A., et al. 2016, ApJ, 819, 62
Comastri, A., Gilli, R., Marconi, A., Risaliti, G., & Salvati, M. 2015, A&A, 574, L10
Comastri, A., Setti, G., Zamorani, G., & Hasinger, G. 1995, A&A, 296, 1
De Luca, A., & Molendi, S. 2004, A&A, 419, 837
Dickey, J. M., & Lockman, F. J. 1990, ARA&A, 28, 215
Elvis, M., Civano, F., Vignali, C., et al. 2009, ApJS, 184, 158
Fukada, Y., Hayakawa, S., Kasahara, I., et al. 1975, Natur, 254, 398
Gendreau, K. C., Mushotzky, R., Fabian, A. C., et al. 1995, PASJ, 47, L5
Gilli, R., Comastri, A., & Hasinger, G. 2007, A&A, 463, 79
Gilli, R., Risaliti, G., & Salvati, M. 1999, A&A, 347, 424
Gilli, R., Salvati, M., & Hasinger, G. 2001, A&A, 366, 407
Gruber, D. E., Matteson, J. L., Peterson, L. E., & Jung, G. V. 1999, ApJ, 520, 124
Hasinger, G. 2008, A&A, 490, 905
Helgason, K., Cappelluti, N., Hasinger, G., Kashlinsky, A., & Ricotti, M. 2014, ApJ, 785, 38
Hickox, R. C., & Markevitch, M. 2006, ApJ, 645, 95
Hickox, R. C., & Markevitch, M. 2007, ApJL, 661, L117
Hopkins, P. F., Richards, G. T., & Hernquist, L. 2007, ApJ, 654, 731
Humphrey, P. J., Liu, W., & Buote, D. A. 2009, ApJ, 693, 822
Ilbert, O., Capak, P., Salvato, M., et al. 2009, ApJ, 690, 1236
Kashlinsky, A. 2016, ApJL, 823, L25
Kashlinsky, A., Arendt, R. G., Ashby, M. L. N., et al. 2012, ApJ, 753, 63
Kinzer, R. L., Jung, G. V., Gruber, D. E., et al. 1997, ApJ, 475, 361
Laigle, C., McCracken, H. J., Ilbert, O., et al. 2016, arXiv:1604.02350
Leccardi, A., & Molendi, S. 2007, A&A, 472, 21
Marchesi, S., Civano, F., Elvis, M., et al. 2016, ApJ, 817, 34
Markevitch, M., Bautz, M. W., Biller, B., et al. 2003, ApJ, 583, 70
McCammon, D., Almy, R., Apodaca, E., et al. 2002, ApJ, 576, 188
Miyaji, T., Ishisaki, Y., Ogasaka, Y., et al. 1998, A&A, 334, L13
Moretti, A., Campana, S., Lazzati, D., & Tagliaferri, G. 2003, ApJ, 588, 696
Moretti, A., Pagani, C., Cusumano, G., et al. 2009, A&A, 493, 501
Moretti, A., Vattakunnel, S., Tozzi, P., et al. 2012, A&A, 548, A87
Pacucci, F., Ferrara, A., Grazian, A., et al. 2016, MNRAS, 459, 1432
Pacucci, F., Ferrara, A., Volonteri, M., & Dubus, G. 2015, MNRAS, 454, 3771
Puccetti, S., Vignali, C., Cappelluti, N., et al. 2009, ApJS, 185, 586
Revnivtsev, M., Gilfanov, M., Sunyaev, R., Jahoda, K., & Markwardt, C. 2003, A&A, 411, 329
Salvaterra, R., Haardt, F., Volonteri, M., & Moretti, A. 2012, A&A, 545, L6
Scoville, N., Abraham, R. G., Aussel, H., et al. 2007a, ApJS, 172, 38
Scoville, N., Aussel, H., Brusa, M., et al. 2007b, ApJS, 172, 1
Shankar, F., Weinberg, D. H., & Miralda-Escué, J. 2009, ApJ, 640, 20
Treister, E., Schawinski, K., Volonteri, M., & Natarajan, P. 2013, ApJ, 778, 130
Treister, E., & Urry, C. M. 2005, ApJ, 630, 115
Treister, E., Urry, C. M., & Virani, S. 2009, ApJ, 696, 110
Ueda, Y., Akiyama, M., Hasinger, G., Miyaji, T., & Watson, M. G. 2014, ApJ, 786, 104
Verner, D. A., Ferland, G. J., Korista, K. T., & Yakovlev, D. G. 1996, ApJ, 465, 487
Watanabe, K., Leising, M. D., Hartmann, D. H., & The, L.-S. 1998, AN, 319, 67
Wilms, J., Allen, A., & McCray, R. 2000, ApJ, 542, 914
Worsley, M. A., Fabian, A. C., Barcons, X., et al. 2004, MNRAS, 352, L28
Yue, B., Ferrara, A., Salvaterra, R., Xu, Y., & Chen, X. 2013, MNRAS, 433, 1556